Electronics and Electrical Engineering

AIMS Electronics and Electrical Engineering, 7(4): 243–270.
DOI: 10.3934/electreng.2023015
Received: 16 August 2023
Revised: 26 September 2023
Accepted: 07 October 2023
Published: 17 October 2023

http://www.aimspress.com/journal/ElectrEng

Research article

Analog interface based on capacitance multiplier for capacitive sensors and application to evaluate the quality of oils

Vasileios Delimaras*, Kyriakos Tsiakmakis and Argyrios T. Hatzopoulos

Department of Information and Electronic Engineering, International Hellenic University (IHU), Sindos, Thessaloniki, 57400, Greece

*** Correspondence:** Email: delimaras@gmail.com.

Abstract: Currently, interdigital capacitive (IDC) sensors are widely used in science, industry and technology. To measure the changes in capacitance in these sensors, many methods such as differentiation, phase delay between two signals, capacitor charging/discharging, oscillators and switching circuits have been proposed. These techniques often use high frequencies and high complexity to measure small capacitance changes of fF or aF with high sensitivity. An analog interface based on a capacitance multiplier for capacitive sensors is presented. This study includes analysis of the interface error factors, such as the error due to the components of the capacitance multiplier, parasitic capacitances, transient effects and non-ideal parameters of OpAmp. A design approach based on an IDC sensor to measure the quality of edible oils is presented and implemented. The quality relates to the total polar compounds (TPC) and consequently to relative electrical permittivity ε_r of the oils. A measurement system has been implemented to measure the capacitance of the IDC sensor, which depended on ε_r. The simulation and experimental results showed that, for a capacitance multiplication factor equal to 1000, changes of 3.3 μs/100 fF can be achieved with an acceptable level of noise, which can be easily measured by a microcontroller.

Keywords: analog interface; capacitive sensors; quality of oils; total polar compounds; interdigital capacitor; capacitance multiplier; capacitance-to-time converter

1. Introduction

Nowadays, capacitive sensors are widely used in many areas of science and industry. Simple sensors for humidity, pressure, gases and other physical and chemical quantities [1], as well as more

complex biosensors, such as for the detection of DNA [2], proteins [3], bacteria or cells [4–6], blood analysis [7], water analysis [8] and other biological and medical agents used in biological, medical and other fields of science.

The operating principle is simple, any change in the material under test (MUT), which is used as the dielectric material of a capacitor structure, such as the interdigital capacitor (IDC) structure, will change the relative electrical permittivity (ε_r), and consequently, the capacitance of the structure.

Several methods have been proposed to measure the capacitance of similar structures [9–12], such as the double differential principle [13], differential measurement with current sense amplifiers [14], RC phase delay [15], charging and discharging method [16,17], oscillators [18,19], capacitance-to-phase converters [20], capacitance-to-frequency (C/F) converters [6,21], capacitance-to-time (C/T) converters [22–31], switched-capacitors (SC) and the charge-transfer method [18,32,33]. Some of these methods use frequencies from kHz to MHz, higher frequencies for small capacitance measurements [9–12,26,27,31,35], and some of them implemented in CMOS technology [6,9–12,26,27] are more complex. Direct sensor-to-microcontroller interfaces have the advantage of simplicity but are used to measure capacitances of tens and hundreds of pF [17], or with a specific algorithm to reduce the range to 1 pF on high frequency [35]. Simple ring and relaxation oscillators to measure the capacitance lower than 2 pF need a large value of resistor, even in MΩ range [27,31,32,36], which is more vulnerable to noise. Also, operational amplifiers (OpAmp) with high SR (slew-rate) and GB (gain bandwidth) are needed, as well as high-speed comparators [34,37]. RC relaxation oscillators exhibit non-linear behavior owing to the inverse relationship between capacitance and frequency [34,37]. In particular, for capacitances of several pF, non-linearity was observed, as reported in [30]. Other techniques employ operational transconductance amplifiers (OTAs) or transimpedance amplifiers (TIAs) to measure capacitance below 1 pF [9–12,24,29]. High-performance methods, such as the capacitance-to-digital (C/D) converter [9–12], employ complex circuits integrated into CMOS technology [9–12,29–31]. In reference [38], an application for real-time monitoring of transformer oil condition was presented, using the AD7150. As an IC, it is a more complex circuit and typical works in the excitation frequency of 32 KHz as specified in its datasheet. The ICs in the AD7745/46/47 and AD7150/51/52/53 families exhibit a limited capacitance range, typically up to 20 pF [32].

In this study, the use of a capacitance multipliers are studied and used as the main stage for the implementation of a novel capacitance measuring technique with high sensitivity classified within the C/T converter category. Wide ranges of capacitances, from fF to μF can be measured. It can detect small changes in capacitance without the need for high frequencies, switching devices or more complex circuits.

Following that, the implementation of this method will be presented through an application for measuring the quality/degradation of edible oils or other liquid MUT, such as lubricant oils. According to [39–41], the increase of Total Polar Compounds (TPC) in edible oils due to their repeated thermal process is an indicator of their degradation and quality. Kumar et al. [42] showed that the electrical properties of oils can be used as indicators of the condition and quality of edible oils because they are inherently dependent on TPC and are well correlated with physical properties such as the viscosity of the oils.

Pérez and Hadfield [43] demonstrated that the same applies to lubricating oils, and can be used to estimate their quality. The authors implemented a sensor and high-frequency analog interface using CFA (current feedback amplifier) to measure the capacitance of the sensor.

These physical and chemical changes indicate the degradation of edible or lubricating oils, and are expressed as changes in the relative complex electrical permittivity ε_r^* of the oils.

Thus, oils are the MUT to be measured, which are placed on the surface of an IDC sensor. According to [43], changes in the relative complex electrical permittivity ε_r^* of the oils will also change the total capacitance of the sensor, in our case the IDC.

Pérez and Hadfield [43], shows that the electrical permittivity is equal to (1):

$$\varepsilon_r^* = \frac{\varepsilon^*}{\varepsilon_0} = \varepsilon_r^{'} - j\varepsilon_r^{''} = \left(\frac{\varepsilon^{'}}{\varepsilon_0}\right) - j\left(\frac{\varepsilon^{''}}{\varepsilon_0}\right) \quad (1)$$

where $\varepsilon_r^{'}$ is the real part of the relative complex electrical permittivity and represents the energy storage, while respectively $\varepsilon_r^{''}$ is the imaginary part and expresses the losses of the dielectric material. In lubricating oils $\varepsilon_r^{'} \gg \varepsilon_r^{''}$, and in low frequencies the electrical permittivity has higher variations. Thus, the sensitivity of the sensor is higher when the measurement frequency remains constant. In the proposed circuit, the operation principle of measuring the capacitance is based on applying the desired adjustable constant DC current to the capacitive sensor to achieve the maximum sensitivity of the measurement circuit and measure the maximum capacitance, because of the effect of the relative complex electrical permittivity, which is maximum at 0 Hz. For certain materials under test on the IDC, such as water [44,45], the real and imaginary parts of (1) strongly affect the measurement capacitance and decrease as the frequency is increased from a few Hz to a few KHz. The authors of [44,45] showed that the measured capacitance of water can be dramatically changed in the range of 100 Hz to 2 KHz. Consequently, some materials under testing require extremely low frequencies (or 0 Hz) to measure the maximum capacitance with the highest attainable sensitivity.

The proposed circuit comprises a widely used 555 timer configured as a monostable multivibrator specifically designed to operate with DC current. A capacitance multiplier circuit and an adjustable constant current source are provided on a 555 timer as a novel modified monostable multivibrator to extend the capability of capacitance measurement circuits, enabling them to effectively measure capacitances as low as a few fF or even aF while maintaining high sensitivity. A constant current source is chosen because is more immune to noise. Additionally, the capability to adjust the desired current allows for control over the chosen measurement range within which the sensor operates, enabling a wide measurement range spanning from fF to μF. These changes adapt the circuit for measuring the capacitance of any tested material. Remarkably, this level of performance is comparable, if not superior, to more complex circuits. Additionally, this circuit is simple and cost-effective, necessitating only one OpAmp, three resistors and a single transistor in its basic configuration. It can be easily implemented using discrete components.

In the subsequent sections of this paper, we elaborate on a simple modification of the capacitance multiplier, which enhances the accuracy of the capacitance measurement circuit, and also elaborate on the error sources in measurement and linearity. This novel circuit and modification also offers the flexibility to easily upgrade existing monostable or astable multivibrator circuits, enabling them to operate effectively in scenarios involving low capacitances, whether using a constant current source or a voltage source.

2. Materials and methods

The basic concept of the proposed capacitance-to-time converter (CTC) circuit illustrated in Figure 1 consists of a constant current source to provide more immunity to noise that linearly charges

the capacitive sensor C_x and, with the help of a timer, the charging time is converted into a pulse of the same duration as that of the charging time.

Sensor C_x is linearly charged up to the timer threshold. Depending on the timer used, the threshold can be adjusted by using one of its terminals.

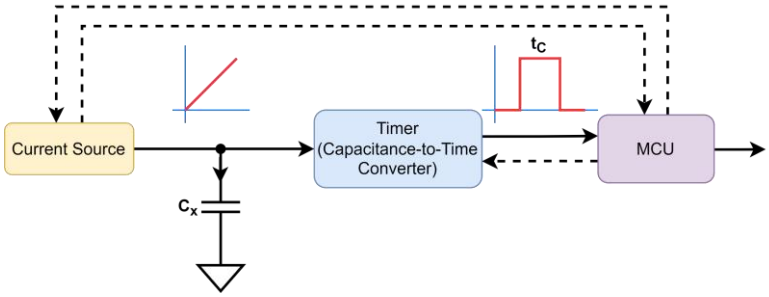

Figure 1. Block diagram of the operating principle. The current source charges C_x. The timer, as a monostable multivibrator, produces an output pulse of time duration t_C as long as the charging duration. Optionally, the current source can be adjusted and monitored by the MCU. The measurement period (time where the measurement starts) is controlled by the MCU and remains constant.

The 555 timer is a highly popular, exceptionally versatile and widely used analog IC. Its utility spans a diverse range of applications in electronic circuits, remaining a subject of ongoing research interest to this day, frequently incorporated as a component part in novel circuit designs [46].

Common circuits with the 555 timer as shown in Figure 2 are simple and work well for high values of capacitance C_x. However, when the capacitance C_x becomes sufficiently small, as is the actual capacitance of an IDC sensor, the input parasitic capacitances of the circuit components become comparable or even higher than the capacitance we want to measure, which creates problems in the operation of the circuit and errors introduced in the charging time measurements.

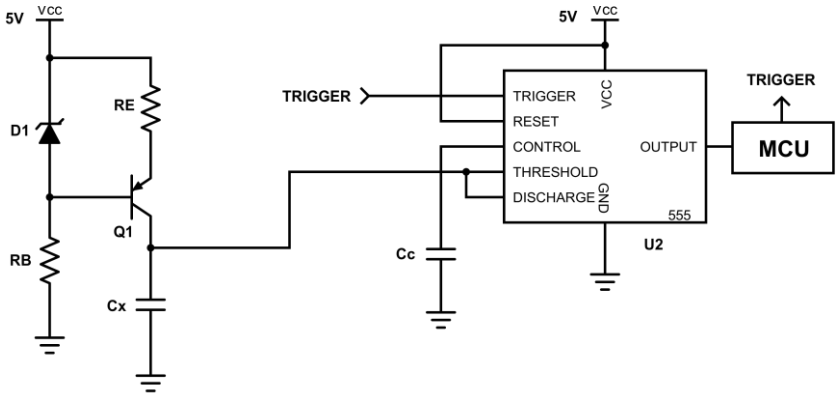

Figure 2. Typical CTC circuit with 555 timer as a monostable multivibritor and current source implemented with BJT (bipolar junction transistor).

The parasitic capacitances are connected in parallel to the capacitance of the sensor and form a current divider with respect to the current source. This means that the charging current of C_x becomes significantly different (smaller) from the desired value when the parasitic capacitances have a value

comparable to that of C_x. The total capacitance that will eventually be charged is $C_x + C_{stray}$, with C_{stray} being the parasitic capacitances.

The simulation results using OrCAD PSpice for capacitance C_x at 10 nF and 5 pF are shown in Figure 3. For the case of 5 pF, the charging current is no longer the desired one. Hence, the charging time of the capacitance is different than expected. The constant current source was set to 100 μA; however, as depicted in Figure 3(b), the current through capacitor C_x is non-constant and does not exceed 6.6 μA.

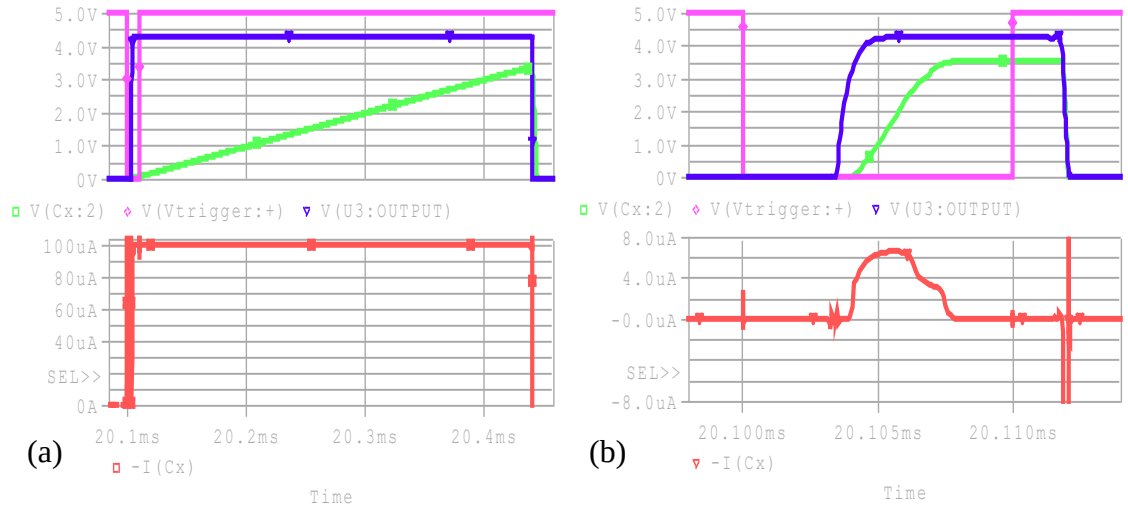

Figure 3. (a) Charging period of the capacitor C_x = 10 nF is observed at the top. The voltage variation across C_x is shown in the form of a ramp (green line). It is also noticed that the positive logic output pulse of the monostable multivibrator (blue line), as well as the trigger signal of the monostable multivibrator (magenta line). Bottom figure shows the constant current through C_x; (b) The corresponding figures pertain to the case in which the capacitor C_x = 5 pF.

The aforementioned reasons indicate that common and simple circuits utilizing the 555 timer are not suitable for accurately measuring small capacitances. Various alternative techniques have been developed to address this issue. In this work, the proposed circuit retains the simplicity of a typical 555-based capacitance measurement circuit with excellent linearity. Avoiding the use of oscillators, switched capacitor methods, complex switch topology, large MΩ resistors susceptible to noise, TIA or CFA configurations or other more complex techniques.

2.1. Capacitance multiplier

In order to measure very low capacitance values (pF or fF) at low frequencies, a capacitance-to-voltage (CTV) converter, which consists of a capacitance multiplier and a constant current source, is used. The capacitance multiplier is a circuit that behaves as a multiplier of the capacitance C_x and is shown in Figure 4(a).

The resulting equivalent circuit is illustrated in Figure 4(b), where the equivalent capacitor C_x' appears to charge from V_{in} through resistor R_S.

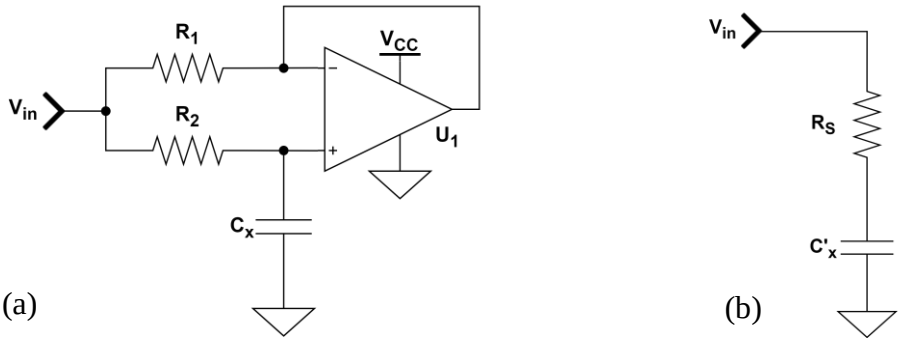

Figure 4. (a) Typical Capacitance Multiplier implemented with OpAmp; (b) Equivalent circuit.

The resulting equivalent capacitance $C_x^{'}$ and resistor R_S are equal to:

$$C_x^{'} = C_x \frac{R_2}{R_1} \qquad R_S = R_1 \| R_2 \tag{2}$$

The total current from V_{in} is the sum of the currents I_1 and I_2 through resistors R_1 and R_2, respectively. The current I_2 is $R_2 \,/\, R_1$ times smaller than I_1. The current of the equivalent capacitor is I_1. Current I_2 creates a voltage drop across resistor R_2 and is an error factor in the circuit. Ignoring this error, the equivalent capacitor charges at input voltage V_{in} start at zero, which is desirable.

If the ratio $R_2 \,/\, R_1$ is very high (greater than 100), R_S can be equal to R_1.

In the case of applying a constant current source with a current I_s through R_s and $C_x^{'}$, I_s is equal to the current of the equivalent capacitance $C_x^{'}$ and is given by:

$$I_s = I_{C_x^{'}} = \frac{dv_{C_x^{'}}}{\mathrm{dt}} C_x^{'} \tag{3}$$

The sum of the voltage drops across R_s and $C_x^{'}$ is denoted as V_{in}. This was determined using Kirchhoff's law and solving (3) for the voltage across $C_x^{'}$. It is time dependent and is given by:

$$V_{in}(t) = I_s R_s + \frac{I_s}{C_x^{'}} \Delta t \tag{4}$$

where Δt is the time elapsed since $C_x^{'}$ is charging linearly.

Similarly, the V_{in} on Figure 2(a) is given by:

$$V_{in}(t) = I_2 R_2 + \frac{I_2}{C_x} \Delta t \tag{5}$$

2.2. The overall circuit

Figure 5 shows the overall circuit with the implementation of the capacitance multiplier and use as timer a typical CMOS 555. The circuit's supply voltage is denoted as V_{CC}. The microcontroller (MCU) provides the trigger pulse to begin the charging of C_x (transition of the voltage level at the TRIGGER input below $1/3V_{CC}$). A constant current source causes the charging; optionally, its current can be regulated by the MCU's digital-to-analog converter (DAC). The output of the 555 is HIGH until the voltage drop across C_x exceeds the threshold of $2/3V_{CC}$. Then, capacitor C_x discharges through the internal transistor of 555 and its output switches to LOW. The duration of the output pulse, that is, the charging time t_c, is timed by the MCU.

The estimated value of $\widehat{C_x}$ is calculated from the following, when the current I_s of the linear charge and the charging time t_c are known,

$$\widehat{C_x} = \frac{C_x^{'}}{N} = \frac{\frac{t_c\, I_s}{V_c}}{N} = \frac{t_c\, I_s}{V_c\, N} \tag{6}$$

where $V_c = 2/3V_{CC}$ is the threshold voltage in the CONTROL pin of 555 and $N = R_2/R_1$ is the capacitance multiplication factor.

The voltage waveforms across C_x at charging, across the equivalent $C_x^{'}$ (which is the input voltage of the capacitance multiplier), the trigger signal and the output pulse of the monostable multivibrator, are shown in Figure 6.

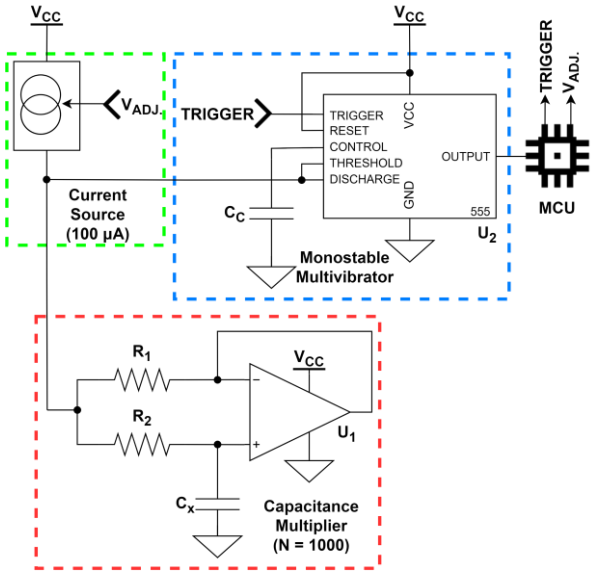

Figure 5. Overall proposed circuit for measuring capacitive sensors. The capacitance multiplier stage was implemented. The constant current source, optionally, can be adjusted and monitored by the MCU.

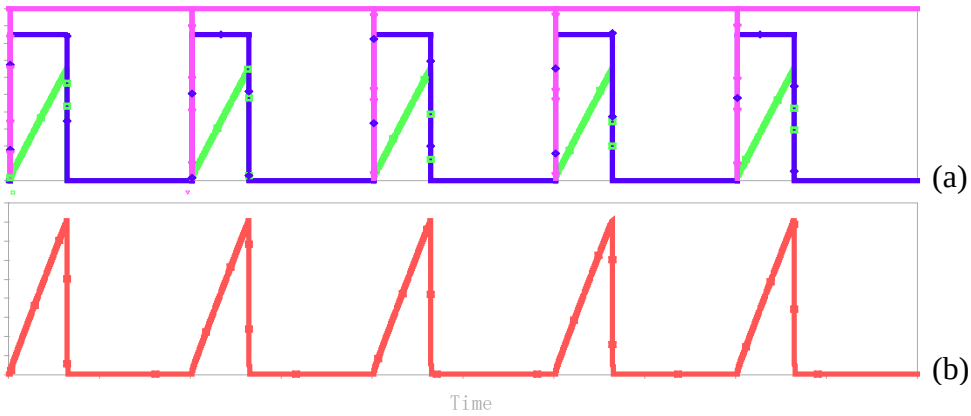

Figure 6. (a) Typical charging periods of the equivalent capacitor $C_x^{'}$ are observed. The voltage variation across $C_x^{'}$ (input of the capacitance multiplier) is shown in the form of a ramp (green line). It is also noticed the output pulse of the monostable multivibrator (blue line), as well as the trigger signal (magenta line) of the monostable multivibrator, which is a pulse of short duration with negative logic, appears at the start of charging; (b) Shows the voltage across the C_x.

3. Measurement errors

The main goal is the measurement of the charging time of the equivalent capacitance $C_x^{'}$ formed by the capacitance multiplier circuit. This time is translated by the monostable multivibrator as the time duration of the output pulse. The measurement errors that can occur are mainly due to the parasitic capacitances of the components connected to the same node as the capacitor C_x, the non-ideal characteristics of the operational amplifier (OpAmp), the transient effect at the beginning of charging and noise.

Charging starts from the voltage $I_s R_s$ to the threshold voltage V_c of the monostable multivibrator. This leads to a shorter charging time than is actually needed. The error introduced by R_s is an initial condition in charging C_x, and consequently, the equivalent $C_x^{'}$.

3.1. Effect of parasitic capacitances

Parasitic capacitances are often connected in parallel to the same nodes as capacitor C_x and equivalent capacitance $C_x^{'}$, causing significant errors.

These are the parasitic capacitances of the threshold and discharge inputs of 555, which are parallel to the equivalent capacitance $C_x^{'}$. In addition, the parasitic capacitance of the non-inverting input of OpAmp is parallel to the capacitor C_x. The circuit that includes parasitic capacitances is shown in Figure 7.

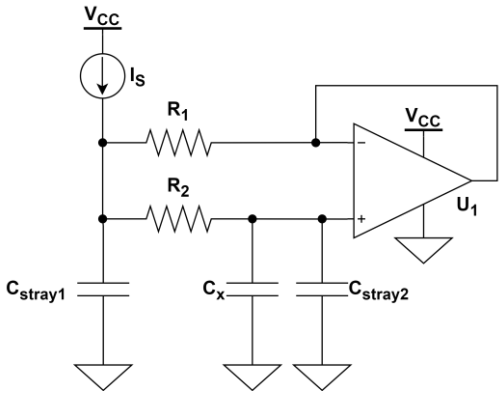

Figure 7. Parasitic capacitances in the Capacitance Multiplier circuit.

$C_{stray\,1}$ is the parasitic capacitance connected in parallel with the equivalent capacitance $C_x^{'}$, and $C_{stray\,2}$ is the parasitic capacitance connected in parallel with the capacitor C_x. The parasitic capacitances of the traces on the PCB connections are added to both $C_{stray\,1}$ and $C_{stray\,2}$ and should be considered as well.

The equivalent unknown capacitance $C_x^{'}$ can be calculated using the following:

$$C_x^{'} = N\left(C_x + C_{stray\,2}\right) + C_{stray\,1} \tag{7}$$

Considering that the values of the parasitic capacitances are in the same order, the impact of $C_{stray\,1}$ is negligible compared to $(C_x + C_{stray\,2})$ as it is multiplied by the large factor N. To face this problem, an OpAmp with very low input parasitic capacitance is chosen. Also, careful design on the PCB level should take place in order to minimize the impact of the conductors that connect C_x with the OpAmp (e.g., be as short as possible to achieve a lower parasitic capacitance).

3.2. Transient phenomena and error caused by non-ideal OpAmp

The transient effect that occurs at the beginning of charging in each measurement cycle, as well as the constant error generated by R_2, creates an initial non-zero voltage condition on the equivalent capacitance $C_x^{'}$, and thus charging starts from this voltage up to $2/3V_{CC}$. This causes the charging time to decrease, as shown in Figure 8, and the result is an underestimation of the capacitance when it is calculated by the microcontroller.

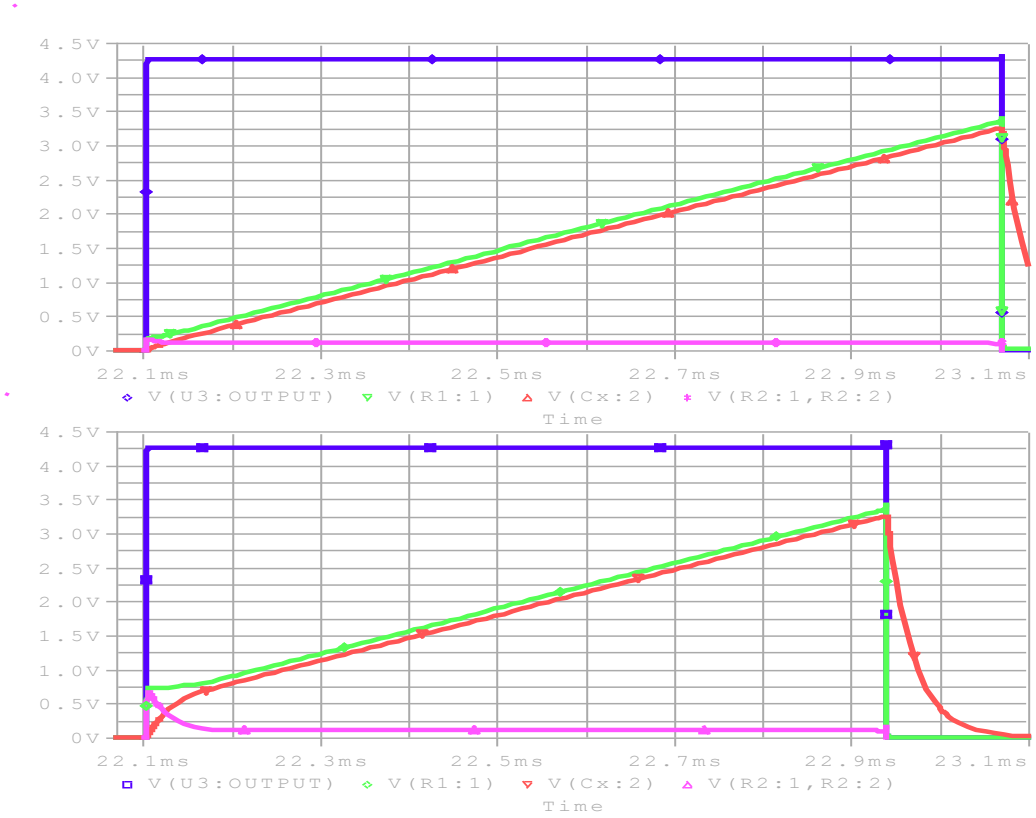

Figure 8. Transient effects affect the duration of the 555-output pulse, and this has the consequence of adding error to the measurement. The bottom graph shows a larger transient effect than the top graph. The magenta line shows the constant error generated by R_2. (I_s = 100 μA, R_1 = 1 KΩ, R_2 = 100 KΩ, C_x = 300 pF)

The minimum output voltage of a non-ideal OpAmp may not be zero when both inputs are shorted together. This is defined by the parameter V_{OL}. When the non-inverting input V_+ is equal to zero, because the capacitor C_x is initially uncharged and the circuit is a voltage follower, the inverting input V_- and the output are equal to V_{OL}. V_{OL} changes when the V_+ input is greater than the V_- input, which is equivalent to V_{OL}.

The equivalent circuit is shown in Figure 9. The superposition theorem is used to calculate the voltage V_{in}, which is equal to $I_2R_2 + V_{OL}$, where $R_2 \,||R_1$ with respect to the current source.

When $V_+ < V_{OL}$, where $V_- = V_{OL}$, C_x is charged exponentially by the voltage source V_{in} after $5R_2C_x$ time constants. When $V_+ > V_{OL}$, the output voltage of OpAmp follows V_+. Consequently, V_+ is equal to V_- and the current source charges C_x linearly.

Because the impact of I_2R_2 is negligible owing to the very high $N = 1000$, the minimum output voltage V_{OL} can be reduced by adding a filter to the feedback of the capacitance multiplier. RC

networks are formed in the circuit, which can cause a transient oscillation effect at the beginning of the charging.

The time constant for the RC network of resistor R_2 in series with capacitor C_x is equal to:

$$\tau = R_2\, C_x \tag{8}$$

and the time constant for the RC network of resistor R_1 in series with the equivalent capacitance $C_x^{'}$ is:

$$\tau' = R_1\, C_x^{'} \tag{9}$$

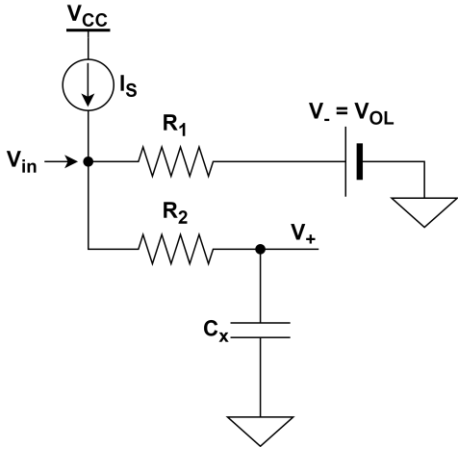

Figure 9. Equivalent circuit for V_{OL} at inverting input.

If $R_2 = NR_1$ and $C_x^{'} = NC_x$, then (8) and (9) will apply:

$$\tau = R_2\, C_x \underset{R_2 = N\, R_1}{\Longrightarrow} \tau = N\, R_1\, C_x \tag{10}$$

$$\tau' = R_1\, C_x^{'} \underset{C_x^{'} = N\, C_x}{\Longrightarrow} \tau' = R_1\, N\, C_x \tag{11}$$

Therefore, $\tau = \tau'$ and these RC circuits are equal.

An additional RC network is formed. It consists of an equivalent capacitance $C_x^{'}$ and a resistor R_2. The time constant τ'' for this network is equal to:

$$\tau'' = R_2\, C_x^{'} \underset{R_2 = N\, R_1}{\Longrightarrow} \tau'' = N\, R_1\, C_x^{'} \tag{12}$$

If an RC circuit is placed in the feedback of the capacitance multiplier, which is equal to or larger than τ'', the transient effect will be eliminated. That is, when:

$$\tau_f = R_3\, C_1 \geq \tau'' = R_2\, C_x^{'} \tag{13}$$

where τ_f is the time constant of the feedback network, while R_3 and C_1 are the feedback components.

The feedback network affects the value of the voltage V_{OL}. Resistors R_3 and R_1 form a voltage divider with respect to V_{OL}. Hence, the inverting input voltage and the error introduced by V_{OL} are decreased. Therefore, the non-inverting input should only exceed a fraction of the value of V_{OL}. The capacitance multiplier based on the $R_3\, C_1$ network is shown in Figure 10.

An improvement in linearity at the start of charging was observed using the $R_3\, C_1$ feedback network, as shown in Figure 11(b). The only remaining error is that due to $I_2 R_2$. The error from $I_2 R_2$

can be reduced by decreasing the R_2 value. The N factor remains constant when R_1 is adjusted properly.

The capacitance C_x is variable, as is $C_x^{'}$ (the variability of C_x leads to the variability of $C_x^{'}$). Therefore, the constant feedback network induces an error in the circuit because the capacitor C_1 of the feedback network has a constant value.

To avoid this error, condition (13) should be applied for the maximum variation of $C_x^{'}$. That is, $C_1 \geq C_{x(max)}^{'}$, since $R_3 = R_2$. In this case, the pulse width at an output of 555 is closer to the expected value.

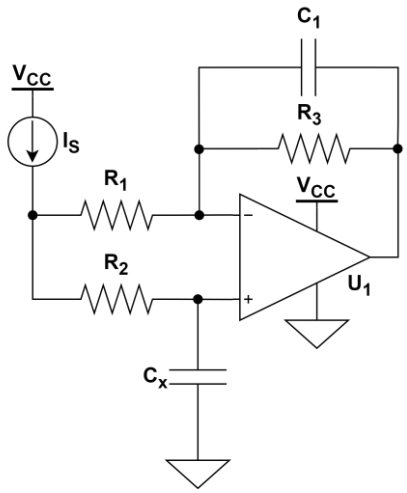

Figure 10. Capacitance multiplier with the $R_3\,C_1$ network in the feedback to eliminate transient effects and reduce the V_{OL} error. ($R_3 = R_2,\ C_1 = C_x^{'}$).

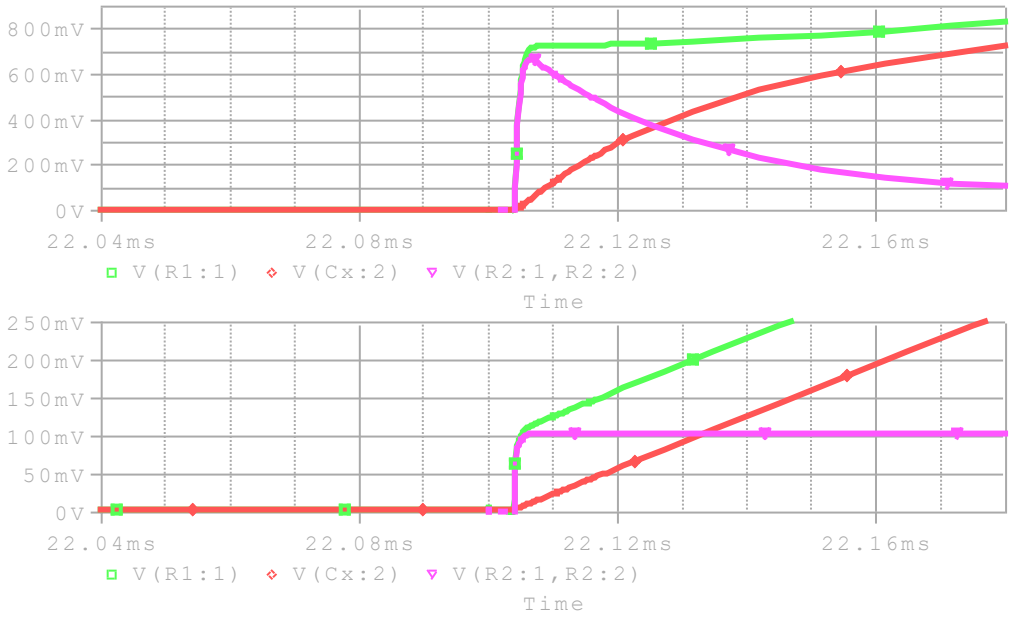

Figure 11. (a) The transient effect at the beginning of capacity charging is observed without the use of the R_3C_1 network; (b) The R_3 = 100 KΩ and C_1 = 30 nF feedback network was used, and elimination of the transient effect was also observed. *(I_s* = 100 μA, R_1 = 1 KΩ, R_2 = 100 KΩ, C_x = 300 pF*).*

3.3. Input offset error and V_{OL}

For a single supply operation, the values of the supply rails are 0 V and V_{CC} in OpAmp. However, the minimum possible output V_{OL} of OpAmp may not be 0 V and is given in the manufacturer's datasheet. For the TLC271 used in the capacitance multiplier circuit, the minimum voltage may be non-zero, and in the worst case, $V_{OL(max)} = 50$ mV.

The input offset voltage V_{IO}, owing to the asymmetry of the input bias currents of the OpAmp inputs multiplied by the gain, appears as an output offset voltage.

Combined with the error caused by I_2R_2, this produces a total error in the OpAmp output. The error caused by resistor R_2 is the highest; therefore, it is necessary to eliminate all errors for high precision applications.

By choosing an OpAmp with lower V_{IO} and $V_{OL(max)}$, it is possible to limit or eliminate the error due to asymmetry and the minimum output voltage of the OpAmp.

3.4. Effect of noise

To measure small values of C_x, a high value of the factor N is required so that the duration of the pulse can be measured by the microcontroller. This means that the R_2 resistor needs to be increased; simultaneously, the current through it will decrease, divided by N times. As a result, R_2 becomes very vulnerable to thermal noise and any type of noise. A small current is more sensitive to charge quantization as well as to the noise figure (NF) caused by components in the overall circuit.

In the circuit shown in Figure 12, a noise source at the frequency of the power supply network (50 or 60 Hz) has been added to the circuit and connected in series with the resistor R_2. This noise source represents the susceptibility of the resistor R_2 to noise. The effect of this source on the duration of the output pulses is shown in Figure 13. The period of the TRIGGER signal was set as 12 ms.

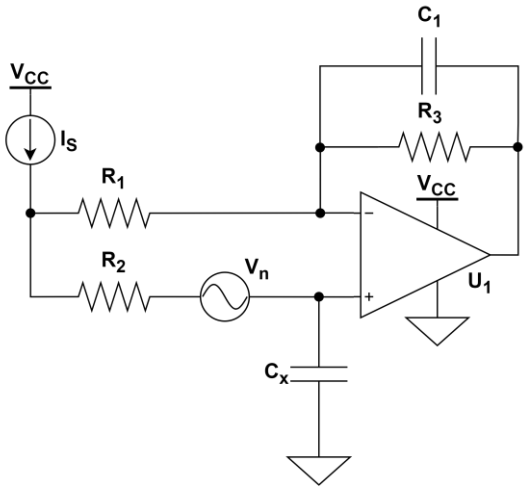

Figure 12. Adding the equivalent noise source to the capacitance multiplier circuit.

When the period of the TRIGGER signal is changed to 20 ms, the noise effect on the circuit remains constant during each charging cycle and, consequently, during the charging time, i.e., the duration of the output pulse. The results are presented in Figure 14.

When the pulse of the TRIGGER signal has the same period as the noise signal ($T_{noise} = 1 / (50\text{ Hz}) = 20$ ms), the noise is sampled and practically captured at the same value as it had or will

have in the previous or next period T. A stable effect of noise in the measurement has been achieved and, consequently, the noise can be eliminated easily, provided that the amplitude of the noise in T does not vary from period to period, and there is no phase difference between the TRIGGER and noise signals.

It should be noted that for short charging times (small values of C_x), a small portion of the noise period will affect the charging signal. The smaller this part is, the more linear the effect tends to become, as shown in Figure 15. For a longer charging time, the effect of noise occurs for a longer period, as shown in Figure 16.

In both Figure 15 and Figure 16, it is observed that increasing the noise voltage reduces the potential difference across the resistor R_2 and results in a reduction of the charging current, thus also increasing the charging time, and vice versa.

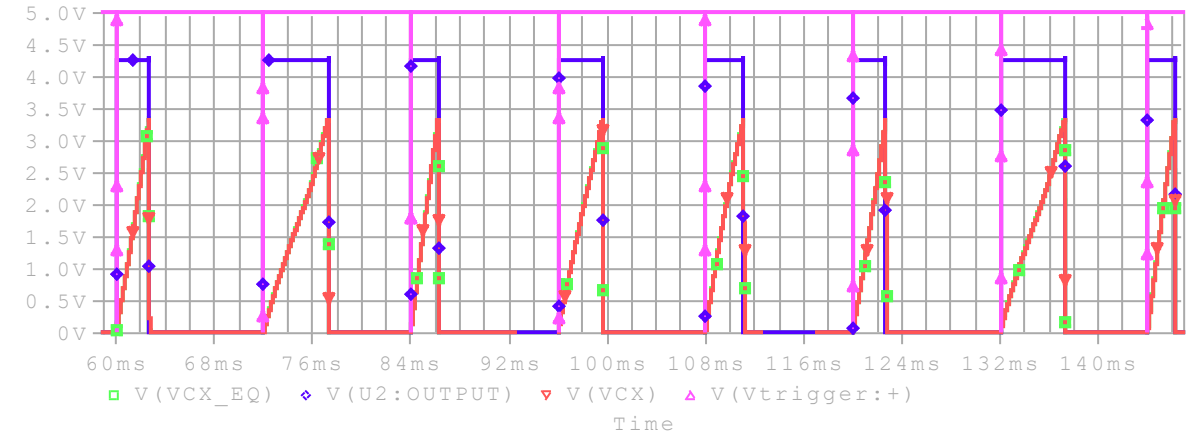

Figure 13. The noise affects the pulse width of the 555's output and varies it according to its amplitude and frequency. ($T_{TRIGGER}$ = 12 ms, I_s = 100 μA, R_1 = 100 Ω, R_2 = 100 KΩ, C_x = 100 pF).

The effect of noise can be stabilized by synchronizing the measurement in the noise frequency and phase. In addition, to limit noise, digital filters can be implemented in the MCU to filter the time values of the output pulse width, i.e., the charging time of capacitor C_x.

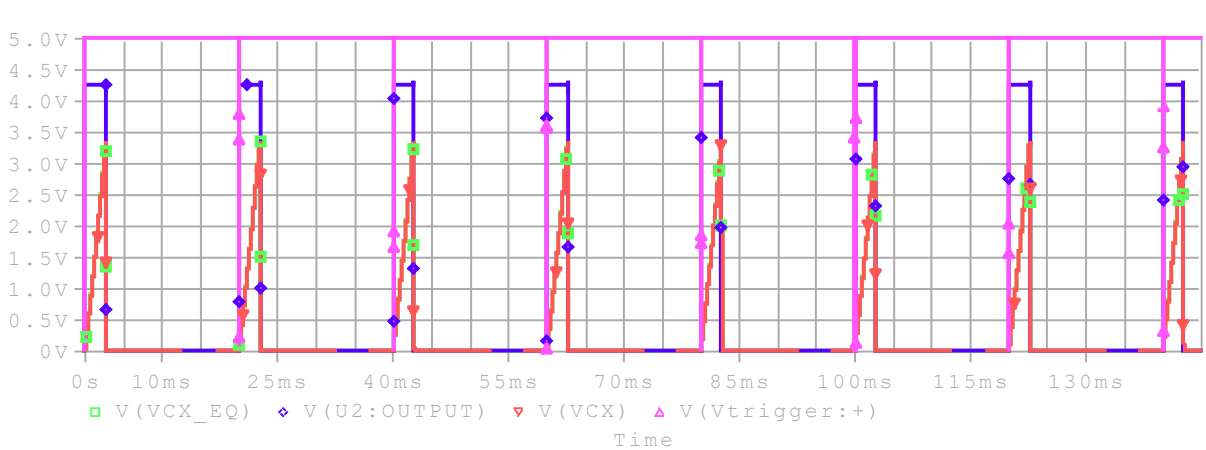

Figure 14. The effect of the noise remains constant during each charging cycle. ($T_{TRIGGER}$ = T_{noise} = 20 ms, I_s = 100 μA, R_1 = 100 Ω, R_2 = 100 KΩ, C_x = 100 pF).

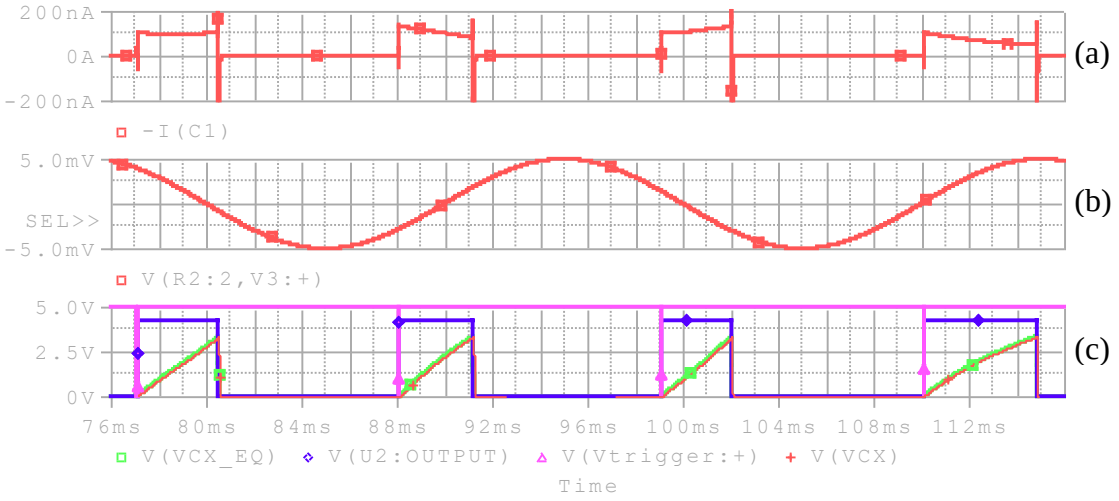

Figure 15. (a) Charging current; (b) noise voltage; (c) charging time and effect of noise. ($C_x^{'}$ = 100 nF, I_s = 100 μA, R_1 = 100 Ω, R_2 = 100 KΩ, C_x = 100 pF).

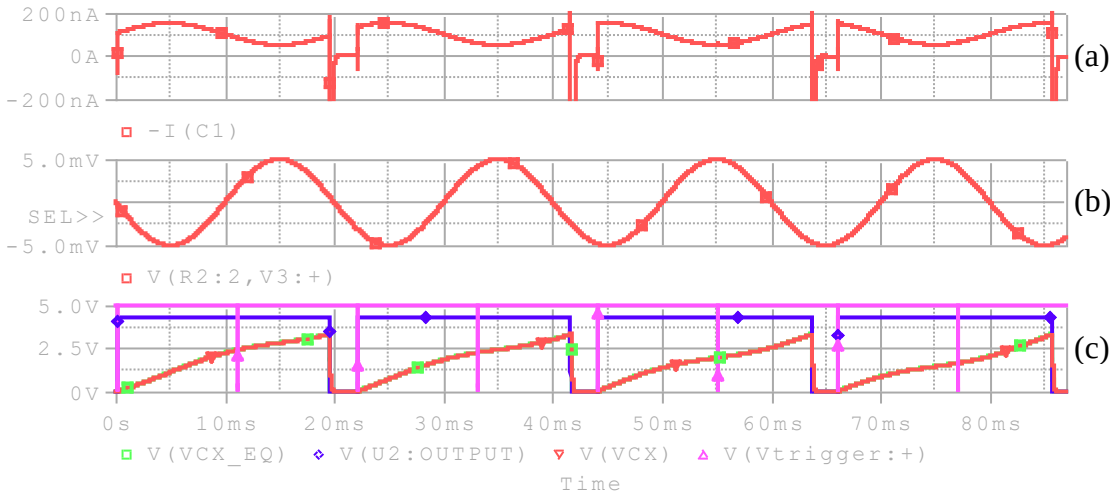

Figure 16. (a) Charging current; (b) noise voltage; (c) charging time and effect of noise. ($C_x^{'}$ = 600 nF, I_s = 100 μA, R_1 = 100 Ω, R_2 = 100 KΩ, C_x = 600 pF).

3.5. Error caused by current source

The current source of the proposed circuit was chosen among four different current source configurations: modified Howland, Wyatt, simple BJT and simple JFET, as shown in Figure 17.

Comparing these configurations of current sources on the maximum load that can be driven, it was found that Howland and simple BJT current sources yield the best results. In the constant current region, current sources are ordered from the highest current stability with respect to the load changes to the lowest, as follows: simple JFET, Howland, and simple BJT current sources. Wyatt current source, on the other hand, exhibits a tendency to significantly diverge as the load increases, rendering it unsuitable for this application.

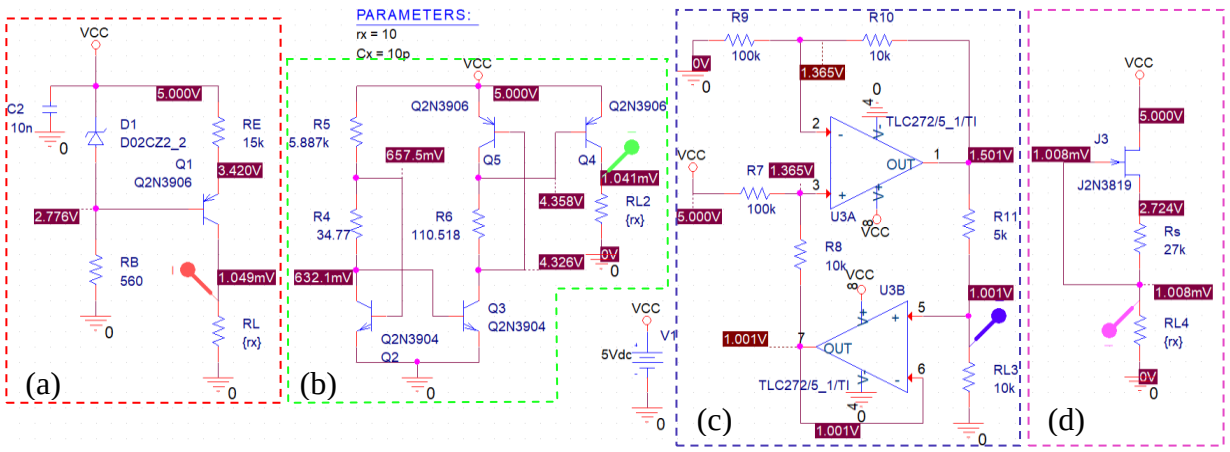

Figure 17. (a) Simple BJT current source; (b) Wyatt current source; (c) Howland type current source; (d) Simple JFET current source.

Another aspect of comparison pertains to the stability of current sources in the constant current region over a temperature range of 0 to 80 ℃. The desired current was set at 100 μA. The results indicate that Howland is more stable than the others with a variation of only 1 nA. However, both the BJT and JFET current sources exhibited relatively small variations in the current within this temperature range. The variations in the desired current were 3.31 μA for the BJT current source, and 5 μA for the JFET current source.

Furthermore, a comparison of the current source stability under varying power supply voltages reveals that the BJT current source is more stable than all other configurations. In contrast, Howland is more sensitive to changes in the power supply voltage. The JFET remains stable, but dramatically reduces the load range in which it can operate as a constant current.

Simple BJT and Howland current sources emerged as optimal choices. However, Howland, in the range of zero to low loads, presented a significant current over the desired current owing to the V_{OL} parameter. Therefore, to ensure simplicity and cost-effectiveness, a simple BJT current source was selected. Any diversion of the desired constant current can be compensated through calibration using a binary search algorithm.

The current source was set to 100 μA using a binary search algorithm based on the output voltage of the ESP32 DAC before initiating the measurement process. Additionally, the power supply voltage V_{CC}, emitter voltage V_E of the current source and 555 threshold voltage V_c were continuously monitored by the ESP32 through its ADC, which was software-linearized for enhanced linearity and accuracy.

The ESP32 internal 8-bit DAC offered a resolution of 12.941 mV. With a maximum error of 1 LSB, the resulting error at the current source was ±0.863%, which is considered acceptable. However, this error can be further reduced by employing an external, high-resolution DAC.

Nevertheless, precise monitoring of V_{CC} and voltage V_E across the emitter resistor R_E (±0.1% tolerance) can eliminate the DAC error, enabling the calculation of current I_s and determination of unknown capacitance C_x with greater accuracy. Therefore, the only errors at the current source introduced by the tolerance of R_E are ±0.99% and from 1 LSB error of the 12-bit ADC to monitor V_{CC} and V_E, whereas in the worst-case scenario it is ±0.0806% for V_{CC} and V_E. The monitored V_c introduces error directly in the capacitance calculations, and is ±0.0244%. The sum of these errors, the total error in current, is ±1.0707%, and all errors affect the capacitance with a total error ±1.0948%. The fixed error of tolerance of R_E is easy to eliminate with a correction factor given by calibration

with low tolerance capacitors to pF or by accurately measuring the R_E value and using this value in calculations for I_S. Thus, the remaining random error that affects the capacitance is only ±0.105% and is caused by ADC. The averaging process described in the next section can reduce this error further.

3.6. Error caused by R_1 and R_2 tolerance

The multiplication factor N is the ratio of R_2/R_1. The change of N evidently affects $C_x^{'}$. According to (5), the tolerance of these resistors affects the current I_2 and thus the charging time t_c. According to (6), this impacts $C_x^{'}$ and finally the calculation of $\widehat{C_x}$.

The tolerance of R_1 and R_2 influence the accuracy of the measurement circuit. Specifically, for $N = 1000$ and 1% tolerance resistors ($R_1 = 100\,\Omega$, $R_2 = 100\,\text{K}\Omega$), in the worst case, the multiplication factor error deviates ±2.02% from the desired value. According to simulations for $C_x = 1$ pF, this introduces ±1.494% error in I_2 and ±1.256% in t_c from the values without tolerance. The total error of $\widehat{C_x}$ becomes ±0.393%. The error caused by resistor tolerance can be reduced with low tolerance resistors, such as 0.1%, which is the same as that used in R_E, or can be eliminated with a correction factor given by calibration with low tolerance capacitors as C_x in pF.

4. Simulation and experimental results

4.1. Simulation results

The capacitor C_c in Figure 5 is replaced by an appropriate resistor. This change causes a decrease in the threshold voltage in the CONTROL pin of 555 from $2/3\,V_{CC}$ to 2.626 V in order to remain within the dynamic input and/or output range of OpAmp.

The simulation results for capacitance variations of C_x from 10 pF to 11 pF, with a step of 100 fF, and for $N = 1000$ are shown in Figure 18. The corresponding changes of the equivalent capacitance $C_x^{'}$ for this range are from 10 nF to 11 nF, with a step of 100 pF.

According to Figure 18, the total pulse width will change incrementally by about 23.49 μs from 10 pF to 11 pF. A change of 1 pF corresponds to approximately 2.35 μs/100 fF. If a wider dynamic range of input and output of an OpAmp is chosen, then changes of 3.3 μs/100 fF can be achieved when the voltage supply remains at $V_{CC} = 5$ V and the threshold voltage in the CONTROL pin of 555 is set to $2/3\,V_{CC}$.

These time variations can be measured easily by a microcontroller. The capacitance C_x of the sensor can then be estimated.

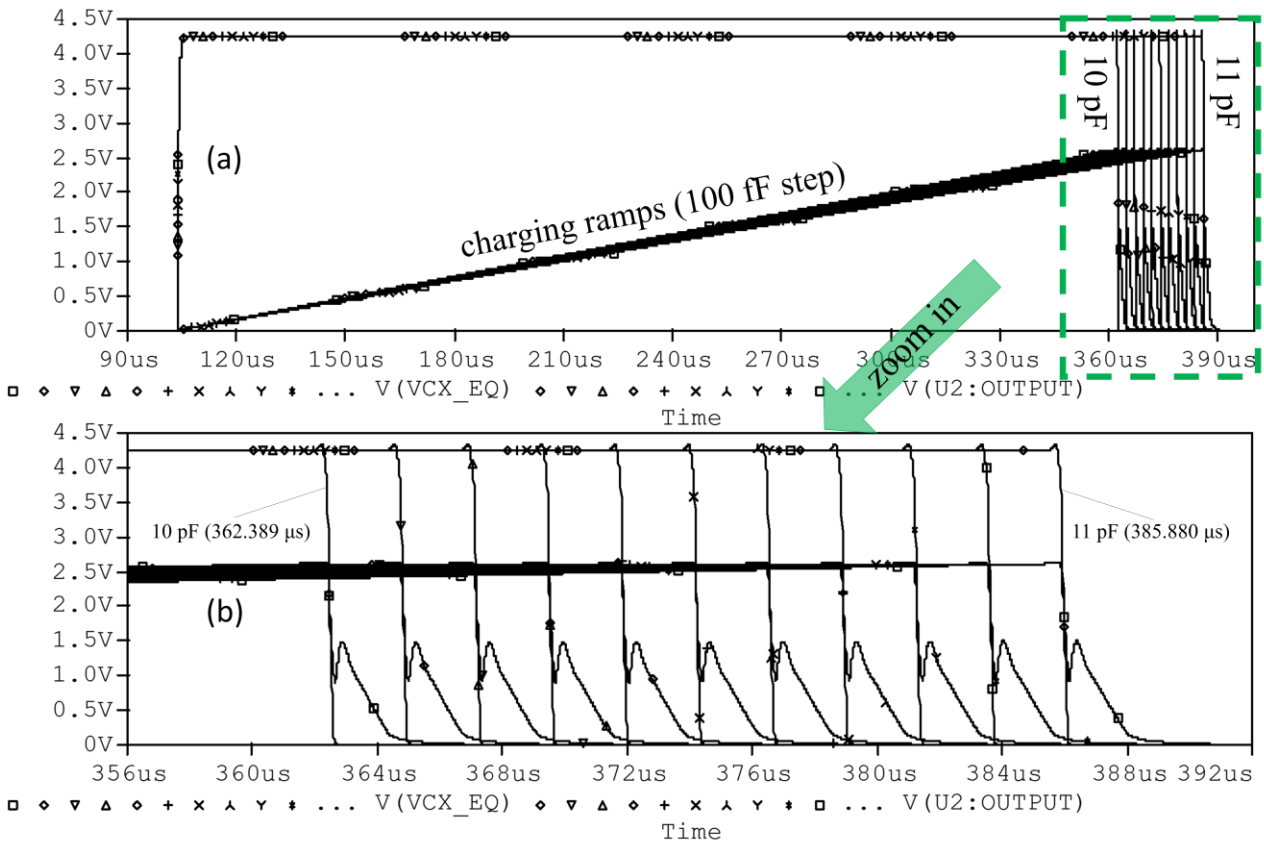

Figure 18. (a) Shows the waveforms of the charge ramp and the output pulse width for capacitance change C_x from 10 pF to 11 pF, with a step of 100 fF and for $N = 1000$, as well as the change in the output pulse width for the range of capacitance changes; (b) The graph focuses on the end of the output pulse width waveforms (area in the rectangle) for each step of the 100 fF change in the range of 10 pF to 11 pF.

4.1.1. Linearity of interface

According to equations (5) and (6), it is expected that the measuring circuit will have a linear response (pulse width) to the changes of the capacitance C_x. Chart the pulse width line $PW_{line}\,(C_x)$ extending from the minimum pulse width value PW_{min} to the maximum pulse width value PW_{max} of the measured pulse width. Following this, determine the discrepancies between $PW_{line}\,(C_x)$ and the measured pulse width data $PW_{measur\,.}(C_x)$. The non-linearity error can be calculated and expressed as:

$$non\_linearity_{error\,\%}(\mathrm{C_x}) = \left|\frac{PW_{line}\,(C_x) - PW_{measur\,.}(C_x)}{PW_{max} - PW_{min}}\right| \times 100\% \tag{14}$$

In the range of 1 pF to 100 pF, a maximum non-linearity of 0.063% is observed, with a notable spike occurring at 30 pF, where the non-linearity reaches 0.085% (the value of $R^2 = 1$), as illustrated by the simulation results in Figure 19.

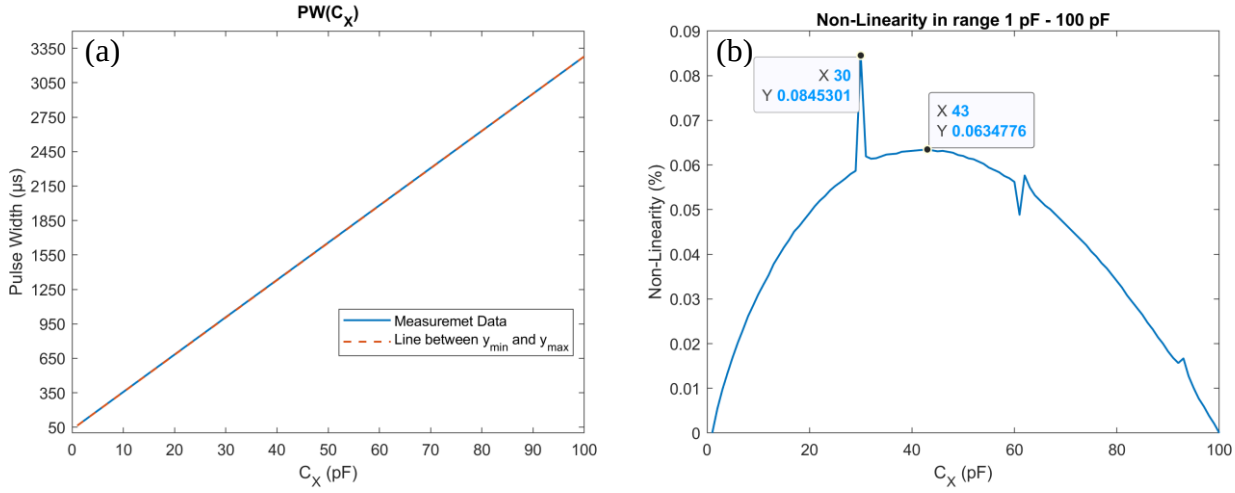

Figure 19. (a) Pulse width and line fit vs C_x changes. Line fit is drawn between $min(C_x)$ and $max(C_x)$; (b) Non-Linearity error percentage in range of 1 pF to 100 pF.

4.2. Experimental results

The experimental procedure used edible sunflower oil that was purchased from a local market. The oil has been divided into eight vials with a 5 ml capacity. Seven of these vials were placed in an oven at a temperature of 200 ℃, below the smoking point of the oil, and one vial was used as a reference for fresh sunflower oil.

Every 2 hours a vial was removed from the oven, and the total time the vial remained in the oven was recorded on the vial label. The last vial was removed after 14 h. The available samples are shown in Figure 20.

Figure 20. Sunflower oil samples. The labels indicate the total time inside the oven for each sample, at a temperature of 200 ℃.

A 200 µl amount of oil from each sample was placed on the surface of the sensor using a precision micropipette. After each measurement, the sensor was cleaned before applying a new sample. Initially, the cleaning process was carried out with isopropyl alcohol; however, in practice, this procedure shifted the initial capacitance value of the sensor for measurement in air, possibly because of the various sorption phenomena occurring on the PCB substrate. Therefore, the cleaning process of the sensor surface was performed by thoroughly wiping it without the use of any solvent. This brings the capacitance of the sensor closer to its initial value.

Measurements of the sensor capacitance charge ramp waveforms and the corresponding 555 output pulse were performed using a SIGLENT SDS 1202X-E oscilloscope. The waveforms are shown in Figure 21.

The experimental setup was designed on a PCB and implemented as an integrated portable device with wireless communication via Bluetooth to transfer the measurements and display them on a smartphone. The device uses an ESP32 microcontroller with built-in wireless communication capabilities. The input time resolution of ESP32 is 12.5 ns at a clock frequency of 240 MHz. According to Eq. (6), the time resolution translates into detectable changes in C_x of 476 aF @ V_c = 2.626 V.

The IDC sensor had an initial capacitance of approximately 9.014 pF when measured in air, i.e., without oil on its surface. The geometrical specifications of the IDC are shown in Table 1.

Table 1. Geometrical specifications of the IDC sensor.

Parameter	Value	Units
Number of fingers (N_F)	12	-
Width of fingers (w)	500	μm
Gap between fingers (g)	409	μm
Gap on the end of fingers (g_E)	470	μm
Active length of fingers (l)	8755	μm
Relative electrical permittivity of the PCB $(\varepsilon_{r(FR4)})$	≈ 4.5	-
Thickness of copper (t)	150	μm
Total thickness of substrate (h_{PCB})	1	mm

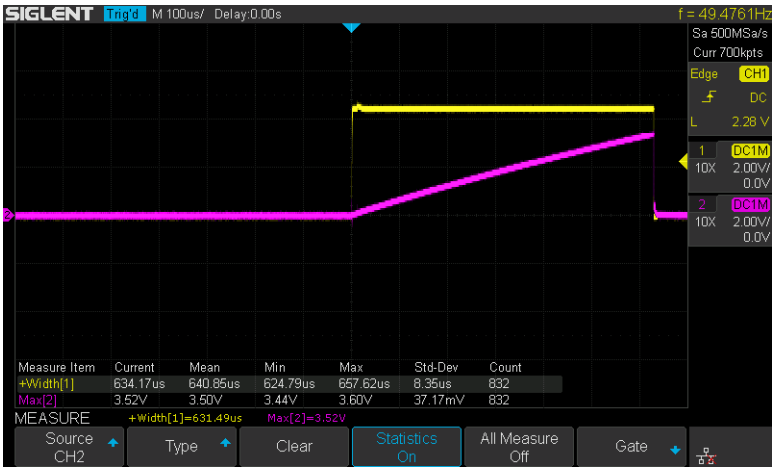

Figure 21. Waveforms of the charge ramp and output pulse width when the sensor is clean (in air, without oil on its surface). The output pulse width has an average value of 640.85 μs ($V_c = 2/3V_{CC}$) in 832 counts of measurements.

The following parameters were used: $N = 1000$ (chosen for the resistor values of the capacitance multiplier: $R_1 = 100\ \Omega$ and $R_2 = 100$ KΩ), $I_S = 100$ μA and the threshold voltage in the CONTROL pin of 555 was set to $V_C = 2.626$ V using an appropriate resistor value. The IDC sensor and the experimental setup as portable device are shown in Figure 22.

The noise standard deviations σ_{n_0} for all the parameters measured by the device (raw data) were calculated and are listed in Table 2. The standard deviation after the averaging procedure was also observed.

The appropriate number of samples for the average was determined using the Allan deviation curve, as shown in Figure 23, for the charging time t_c.

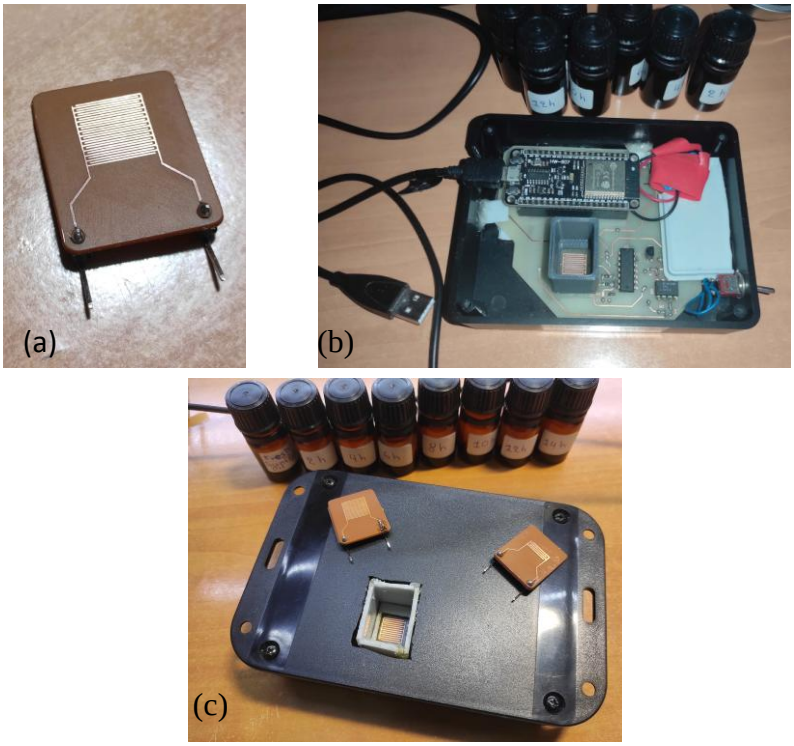

Figure 22. IDC sensor and experimental setup. (a) Individual IDC sensor; (b) ESP32 is used to generate the TRIGGER pulse, control the current source and capture and measure the pulse width of the 555 output; (c) Chamber for the sample to be measured is visible.

Table 2. Initial noise standard deviations for all monitoring parameters and standard deviations after averaging.

Parameter	**Raw Data** σ_{n0}	**Avg. Data** σ_n
Current Source Voltage (V_E)	2.2 mV	0.6 mV
Power Supply Voltage (V_S)	18.8 mV	3.2 mV
Current (I_S)	0.789 μA	0.1376 μA
Charging Time (t_c)	7.3204 μs	0.1277 μs
Sensor Capacitance (C_x)	0.2956 pF	0.0069 pF

All sample measurements were performed at room temperature (24 ℃) using the portable device and are shown in Table 3. 10,000 measurements were taken using ESP32. Outlier values exceeding two standard deviations were replaced, and an average of 10,000 valid measurements were calculated. The data is sent via Bluetooth to a smartphone.

An application using Android Studio was developed to communicate with the portable device and measure the duration of the TIMER output pulse, as well as other system parameters. In addition, the smartphone application was used to start the calibration process, and the current source was set to 100 μA from the output voltage of the ESP32 DAC by using a binary search algorithm, before starting the measurement process.

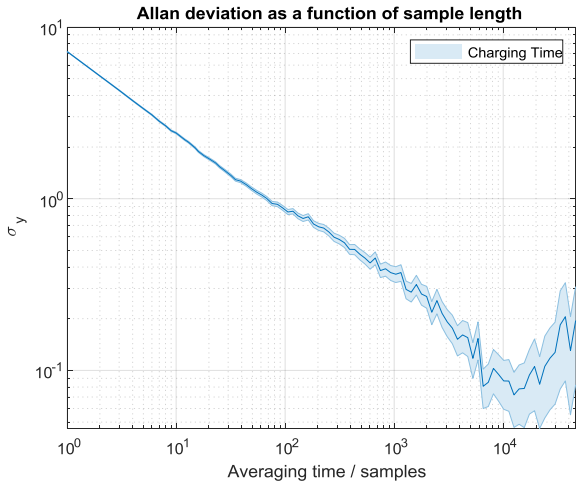

Figure 23. Allan deviation curve as a function of sample length for the charging time t_c. 10,000 samples were appropriate to minimize the standard deviation of the noise.

Table 3. The pulse width measurements of the sunflower oil samples and the initial pulse width values of the sensor when were measured in the air.

Time	Pulse Width	Init. Pulse Wid. (Sensor in air)
0 Fresh Sun. Oil	272.16 μs	236.71 μs
2 h	272.26 μs	236.85 μs
4 h	272.01 μs	236.87 μs
6 h	272.62 μs	236.92 μs
8 h	272.42 μs	236.61 μs
10 h	272.81 μs	236.63 μs
12 h	272.93 μs	236.67 μs
14 h	272.93 μs	236.64 μs

The experimental protocol can be summarized in the following steps: (a) Cleaning the IDC surface, (b) calibrate the constant current source to the desired current, (c) perform 10,000 measurements using an ESP32, outliers are rejected and replaced with new values, then averaging to calculate the capacitance of the IDC, (d) capacitance and other parameters of the circuit sent to a smartphone via Bluetooth, (e) 200 μl of oil sample was placed on IDC surface and (e) measure the new capacitance affected by the oil sample as described in (c). These steps are repeated for each new oil sample. The capacitance of oil samples was compared to that of fresh oil.

Figure 24 shows the corresponding graph of the measurements (pulse duration/width time), which appears as a light orange line. The light blue line represents the measurements where the difference between every initial value of the sensor before each measurement takes place and the initial reference value before the first sample (i.e., fresh sunflower oil) is taken into account. This difference

is added algebraically to each pulse width time measurement to remove any offset error of the initial value of the sensor from the measurement. This error was caused by the non-exact repeated cleaning process, in which the initial capacitance value of the sensor shifted slightly each time.

The estimated capacitance of the IDC sensor for the respective measurements has been calculated using (6) and is also presented in Figure 24. The light orange and light blue lines for the time measurements and the orange and blue lines for the corresponding calculated capacitances of the sensor are shown in the graph.

The blue line in Figure 24 shows that the capacitance decreases and does not follow the expected increase, owing to the formation of polar compounds (increase in TPC), which occurs from time 0 to 4 hours. This probably occurred because of the decrease in moisture and the amount of water contained in the oil, simultaneously with the increase in TPC. The presence of water and moisture in the sample, owing to the high relative electrical permittivity of water ($\varepsilon_r \cong 80$ @ 20 ℃), significantly varies the total capacitance of the sensor, and as it evaporates from the sample, the capacitance decreases. Once the water evaporated, which seems to occur after 4 hours, an increase in capacitance is observed, as expected, to follow the increase in TPCs.

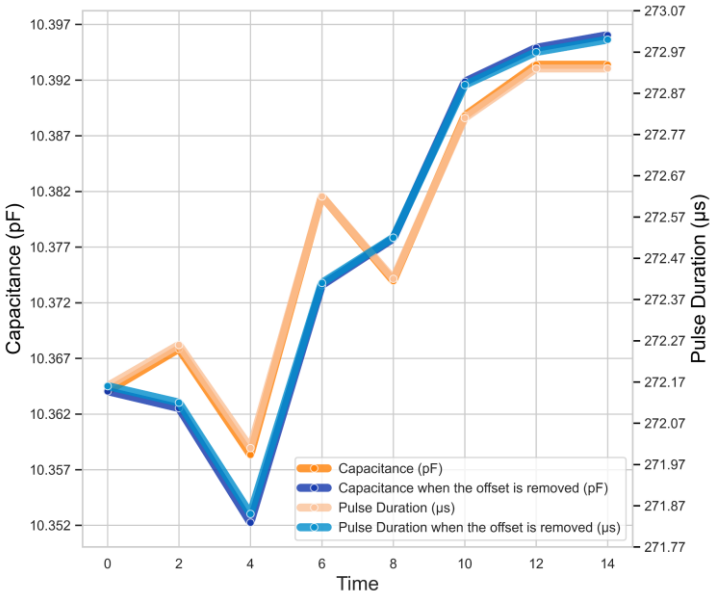

Figure 24. Pulse width measurements for the available samples (light orange line) and pulse width measurements, to which the difference between the initial pulse width before each measurement and the reference initial pulse width before the fresh sunflower oil take place, were algebraically added to the pulse width for each measurement (light blue line). The orange and blue lines represent the corresponding calculated capacitance values.

Scatter plots and box plots depict the distribution of the measurements for the IDC sensor's minimum and maximum values, as depicted in Figure 25. Sensor repeatability was also calculated, with a value of 0.01436 observed within the 9 - 10 pF range.

Table 4 presents a comparison of the sensitivity of the proposed method with that of previous studies on capacitance-measurement circuits based on capacitance-to-period (time) converters.

Table 4. Performance comparison with previous work based on a capacitance-to-period (time) converter.

Reference	Sensitivity	Resolution	Year
(Ramfos and Chatzand., 2012) [22]	0.89 µs/pF (max.)	depending on T_{xtal}	2012
(Bruschi et al., 2008) [23]	30.97 µs/pF	16 fF	2008
(Nizza et al., 2013) [25]	32 µs/pF	800 aF	2013
(Arefin et al., 2016) [26]	3.62 µs/pF (max.)	10.77 aF	2016
(Lu et al., 2011) [27]	7 µs/pF	50 aF	2011
(Brookhuis et al., 2015) [28]	0.49 µs/pF	2 fF	2015
(De Marcellis et al., 2019) [36]	1 µs/pF	83 fF	2019
Proposed	26.26 µs/pF (adj.)	476 aF (default)	2023

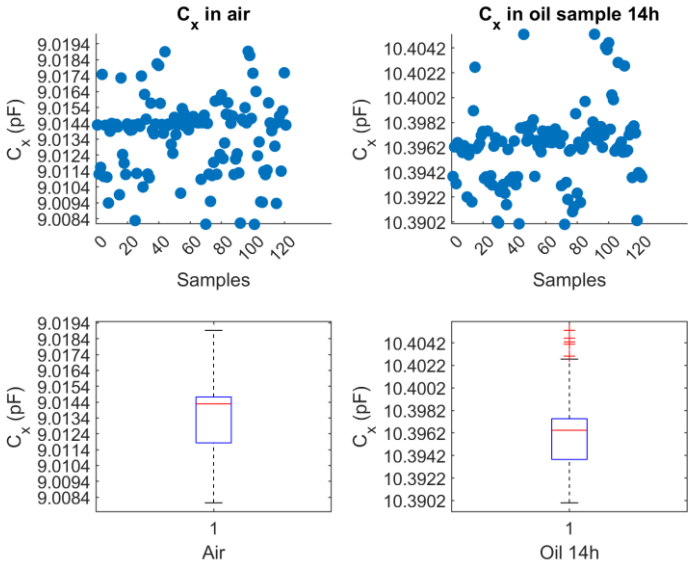

Figure 25. Scatter plots and corresponding box plots for IDC in the air (minimum value), and with oil sample 14h (maximum value).

In this study, the sensitivity was adjustable and defined by the factor N of the capacitance multiplier. The comparison in Table 4 refers to the single-sensor measurements. The resolution of the proposed interface depends directly on the microcontroller clock and can be improved further.

The measurement range can be adjusted with two degrees-of-freedom (DoF) by varying the current supplied by the current source and the value of factor N. Specifically, for the system parameters set at $I_s = 100$ µA and $N = 1000$, the theoretical lower value that can be measured is 476 aF, dependent upon the time resolution (clock) of the ESP32 or any other microcontroller. Zero sensor dead-zone was observed.

The influence of noise negatively affects the limit-of-detection (LoD) and the limit-of-quantification (LoQ). Noise stands as the primary limiting factor, particularly when I_2 is extremely low, owing to a desired reduction in I_s and/or a high value of the N factor, such as 10,000. Consequently, calculation of the LoD and LoQ becomes necessary. The LoD can be expressed as follows:

$$LoD = \frac{3.3\sigma}{s} \tag{15}$$

where σ is the standard deviation of the sensor response in 0.25 pF capacitor (four 1 pF in series), and s is the slope of the calibration process. The concertation of TPCs in oil samples can not be defined without expensive instruments. Common SMD capacitors within the range of 0.25 pF to 10 pF were employed for calibration. Subsequently, 20 final measurements were taken from the interface for each capacitor, and these measurements were averaged to determine the final value. Thanks to the linearity of the sensor, $s \cong 1$ for the output $\widehat{C_x}$ in pF. The LoD is calculated as 0.002090, in pF. The LoQ given by:

$$LoQ = \frac{10\sigma}{s} \tag{16}$$

Similarly, the LoQ value was determined as 0.006334, in pF.

5. Conclusions

An analog interface based on Capacitance Multiplier and an IDC sensor was implemented to measure the quality of edible oils. For $N = 1000$, the noise in the device was at an acceptable level and small differences in the capacitance were measured. Therefore, the oil quality was estimated. The total change in the sensor capacitance for the sunflower oil samples from the initial value of approximately 9.014 pF showed a maximum range of change from 1.338 pF to 1.382 pF for the 14-hour thermal processed pure sample without frying any edible material. The system measured total changes of 44 fF. The output pulse time variation was 1.15 μs/44 fF. The normal usage of frying edible materials with oil is expected to result in higher TPC production as the sensor's capacitance increases, making it more easily measurable. An improvement for a smaller effect of noise and denser structure of the IDC sensor may also allow for higher values of N, such as 10,000, which could further increase the sensitivity of the interface and improve the LoD and LoQ. In future work, the presence of moisture and water in the sample should be eliminated, for example, by thermal treatment or by covering or coating the surface of the sensor with hydrophobic films or polymers that selectively bind the chemical compounds that need to be measured.

Use of AI tools declaration

The authors declare they have not used Artificial Intelligence (AI) tools in the creation of this article.

Conflict of interest

The authors declare that there is no conflict of interest regarding the publication of this paper.

References

1. Khan AU, Islam T, George B, Rehman M (2019) An Efficient Interface Circuit for Lossy Capacitive Sensors. *IEEE Trans Instrum Meas* 68: 829–836. https://doi.org/10.1109/TIM.2018.2853219
2. Wang L, Veselinovic M, Yang L, Geiss BJ, Dandy DS, Chen T (2017) A sensitive DNA capacitive biosensor using interdigitated electrodes. *Biosens Bioelectron* 87: 646–653. https://doi.org/10.1016/j.bios.2016.09.006
3. Mahalingam D, Gurbuz Y, Qureshi A, Niazi JH (2015) Design, fabrication and performance evaluation of interdigital capacitive sensor for detection of Cardiac Troponin-I and Human Epidermal Growth Factor Receptor 2. *2015 IEEE SENSORS - Proc* 1–4. https://doi.org/10.1109/ICSENS.2015.7370209
4. Couniot N, Afzalian A, Van Overstraeten-Schlogel N, Francis LA, Flandre D (2016) Capacitive Biosensing of Bacterial Cells: Sensitivity Optimization. *IEEE Sens J* 16: 586–595. https://doi.org/10.1109/JSEN.2015.2485120
5. Schaur S, Jakoby B (2011) A numerically efficient method of modeling interdigitated electrodes for capacitive film sensing. *Procedia Eng* 25: 431–434. https://doi.org/10.1016/j.proeng.2011.12.107
6. Senevirathna BP, Lu S, Dandin MP, Basile J, Smela E, Abshire PA (2018) Real-Time Measurements of Cell Proliferation Using a Lab-on-CMOS Capacitance Sensor Array. *IEEE Trans Biomed Circuits Syst* 12: 510–520. https://doi.org/10.1109/TBCAS.2018.2821060
7. Claudel J, Ngo TT, Kourtiche D, Nadi M (2020) Interdigitated Sensor Optimization for Blood Sample Analysis. *Biosensors* 10. https://doi.org/10.3390/bios10120208
8. Meng J, Huang J, Oueslati R, Jiang Y, Chen J, Li S, et al. (2021) A single-step DNAzyme sensor for ultra-sensitive and rapid detection of Pb2+ ions. *Electrochim Acta* 368: 137551. https://doi.org/10.1016/j.electacta.2020.137551
9. Ramanathan P, Ramasamy S, Jain P, Nagrecha H, Paul S, Arulmozhivarman P, et al. (2013) Low Value Capacitance Measurements for Capacitive Sensors – A Review. *Sensors & Transducers* 148: 1–10.
10. Ferlito U, Grasso AD, Pennisi S, Vaiana M, Bruno G (2020) Sub-Femto-Farad Resolution Electronic Interfaces for Integrated Capacitive Sensors: A Review. *IEEE Access* 8: 153969–153980. https://doi.org/10.1109/ACCESS.2020.3018130
11. Kanoun O, Kallel AY, Fendri A (2022) Measurement Methods for Capacitances in the Range of 1 pF–1 nF: A review. *Measurement* 195: 111067. https://doi.org/10.1016/j.measurement.2022.111067
12. Forouhi S, Dehghani R, Ghafar-Zadeh E (2019) CMOS based capacitive sensors for life science applications: A review. *Sensors Actuators, A Phys* 297: 111531. https://doi.org/10.1016/j.sna.2019.111531
13. Preethichandra DMG, Shida K (2001) A simple interface circuit to measure very small capacitance changes in capacitive sensors. *IEEE Trans Instrum Meas* 50: 1583–1586. https://doi.org/10.1109/19.982949
14. Haider MR, Mahfouz MR, Islam SK, Eliza SA, Qu W, Pritchard E (2008) A low-power capacitance measurement circuit with high resolution and high degree of linearity. *Midwest Symp Circuits Syst* 261–264. https://doi.org/10.1109/MWSCAS.2008.4616786

15. Dean RN, Rane A (2010) An improved capacitance measurement technique based of RC phase delay. *2010 IEEE Int Instrum Meas Technol Conf I2MTC 2010 - Proc* 367–370. https://doi.org/10.1109/IMTC.2010.5488213
16. Reverter F, Gasulla M, Pallàs-Areny R (2004) A low-cost microcontroller interface for low-value capacitive sensors. *Conf Rec - IEEE Instrum Meas Technol Conf* 3: 1771–1775. https://doi.org/10.1109/IMTC.2004.1351425
17. Czaja Z (2020) A measurement method for capacitive sensors based on a versatile direct sensor-to-microcontroller interface circuit. *Measurement* 155: 107547. https://doi.org/10.1016/j.measurement.2020.107547
18. Van Der Goes FML, Meijer GCM (1996) A novel low-cost capacitive-sensor interface. *IEEE Trans Instrum Meas* 45: 536–540. https://doi.org/10.1109/19.492782
19. Mohammad K, Thomson DJ (2017) Differential Ring Oscillator Based Capacitance Sensor for Microfluidic Applications. *IEEE Trans Biomed Circuits Syst* 11: 392–399. https://doi.org/10.1109/TBCAS.2016.2616346
20. Ashrafi A, Golnabi H (1999) A high precision method for measuring very small capacitance changes. *Rev Sci Instrum* 70: 3483–3487. https://doi.org/10.1063/1.1149941
21. Chatzandroulis S, Tsoukalas D (2001) Capacitance to frequency converter suitable for sensor applications using telemetry, *ICECS'99. Proceedings of ICECS '99. 6th IEEE International Conference on Electronics, Circuits and Systems (Cat. No.99EX357)*, IEEE, 1791–1794. https://doi.org/10.1109/ICECS.1999.814557
22. Ramfos I, Chatzandroulis S (2012) A 16-channel capacitance-to-period converter for capacitive sensor applications. *Analog Integr Circuits Signal Process* 71: 383–389. https://doi.org/10.1007/s10470-011-9738-y
23. Bruschi P, Nizza N, Dei M (2008) A low-power capacitance to pulse width converter for MEMS interfacing. *ESSCIRC 2008 - Proc 34th Eur Solid-State Circuits Conf* 1: 446–449. https://doi.org/10.1109/ESSCIRC.2008.4681888
24. Bruschi P, Nizza N, Piotto M (2007) A current-mode, dual slope, integrated capacitance-to-pulse duration converter. *IEEE J Solid-State Circuits* 42: 1884–1891. https://doi.org/10.1109/JSSC.2007.903102
25. Nizza N, Dei M, Butti F, Bruschi P (2013) A low-power interface for capacitive sensors with PWM output and intrinsic low pass characteristic. *IEEE Trans Circuits Syst I Regul Pap* 60: 1419–1431. https://doi.org/10.1109/TCSI.2012.2220461
26. Arefin MS, Redoutéé JM, Yuce MR (2016) A Low-Power and Wide-Range MEMS Capacitive Sensors Interface IC Using Pulse-Width Modulation for Biomedical Applications. *IEEE Sens J* 16: 6745–6754. https://doi.org/10.1109/JSEN.2016.2587668
27. Lu JHL, Inerowicz M, Joo S, Kwon JK, Jung B (2011) A low-power, wide-dynamic-range semi-digital universal sensor readout circuit using pulsewidth modulation. *IEEE Sens J* 11: 1134–1144. https://doi.org/10.1109/JSEN.2010.2085430
28. Brookhuis RA, Lammerink TSJ, Wiegerink RJ (2015) Differential capacitive sensing circuit for a multi-electrode capacitive force sensor. *Sensors Actuators, A Phys* 234: 168–179. https://doi.org/10.1016/j.sna.2015.08.020
29. Tan Z, Shalmany SH, Meijer GC, Pertijs MA (2012) An energy-efficient 15-bit capacitive-sensor interface based on period modulation. *IEEE J Solid-State Circuits* 47: 1703–1711. https://doi.org/10.1109/JSSC.2012.2191212

30. Li X, Meijer GCM (2002) An accurate interface for capacitive sensors. *IEEE Trans Instrum Meas* 51: 935–939. https://doi.org/10.1109/TIM.2002.807793
31. Gasulla M, Li X, Meijer GCM (2005) The noise performance of a high-speed capacitive-sensor interface based on a relaxation oscillator and a fast counter. *IEEE Trans Instrum Meas* 54: 1934–1940. https://doi.org/10.1109/TIM.2005.853684
32. Yurish SY (2009) Universal Capacitive Sensors and Transducers Interface. *Procedia Chem* 1: 441–444. https://doi.org/10.1016/j.proche.2009.07.110
33. Heidary A, Meijer GCM (2009) An integrated interface circuit with a capacitance-to-voltage converter as front-end for grounded capacitive sensors. *Meas Sci Technol* 20. https://doi.org/10.1088/0957-0233/20/1/015202
34. Liu Y, Chen S, Nakayama M, Watanabe K (2000) Limitations of a relaxation oscillator in capacitance measurements. *IEEE Trans Instrum Meas* 49: 980–983. https://doi.org/10.1109/19.872917
35. Czaja Z (2023) A New Approach to Capacitive Sensor Measurements Based on a Microcontroller and a Three-Gate Stable RC Oscillator. *IEEE Trans Instrum Meas* 72: 1–9. https://doi.org/10.1109/TIM.2023.3244851
36. De Marcellis A, Reig C, Cubells-Beltrán M-D (2019) A Capacitance-to-Time Converter-Based Electronic Interface for Differential Capacitive Sensors. *Electronics* 8: 80. https://doi.org/10.3390/electronics8010080
37. Ulla Khan A, Islam T, Akhtar J (2016) An Oscillator-Based Active Bridge Circuit for Interfacing Capacitive Sensors with Microcontroller Compatibility. *IEEE Trans Instrum Meas* 65: 2560–2568. https://doi.org/10.1109/TIM.2016.2581519
38. Rahman O, Islam T, Khera N, Khan SA (2021) A Novel Application of the Cross-Capacitive Sensor in Real-Time Condition Monitoring of Transformer Oil. *IEEE Trans Instrum Meas* 70. https://doi.org/10.1109/TIM.2021.3111979
39. Khaled AY, Aziz SA, Ismail WIW, Rokhani FZ (2016) Capacitive sensing system for frying oil assessment during heating. *Proceeding - 2015 IEEE Int Circuits Syst Symp ICSyS 2015* 137–141. https://doi.org/10.1109/CircuitsAndSystems.2015.7394081
40. Khamil KN, Mood MAUC (2017) Dielectric sensing (capacitive) on cooking oil's TPC level. *J Telecommun Electron Comput Eng* 9: 27–32.
41. Liu M, Qin X, Chen Z, Tang L, Borom B, Cao N, et al. (2019) Frying Oil Evaluation by a Portable Sensor Based on Dielectric Constant Measurement. *Sensors*: 1–11. https://doi.org/10.3390/s19245375
42. Kumar D, Singh A, Tarsikka PS (2013) Interrelationship between viscosity and electrical properties for edible oils. *J Food Sci Technol* 50: 549–554. https://doi.org/10.1007/s13197-011-0346-8
43. Pérez AT, Hadfield M (2011) Low-cost oil quality sensor based on changes in complex permittivity. *Sensors* 11: 10675–10690. https://doi.org/10.3390/s111110675
44. Behzadi G, Fekri L (2013) Electrical Parameter and Permittivity Measurement of Water Samples Using the Capacitive Sensor. *Int J Water Resour Environ Sci* 2: 66–75. https://doi.org/10.5829/idosi.ijwres.2013.2.3.2938
45. Golnabi H, Sharifian M (2013) Investigation of water electrical parameters as a function of measurement frequency using cylindrical capacitive sensors. *Meas J Int Meas Confed* 46: 305–314. https://doi.org/10.1016/j.measurement.2012.07.002

46. Niranatlumpong P, Allen MA (2022) A 555 Timer IC Chaotic Circuit: Chaos in a Piecewise Linear System With Stable but No Unstable Equilibria. *IEEE Trans Circuits Syst I Regul Pap* 69: 798–810.

AIMS Press